NRIAG JOURNAL OF ASTRONOMY AND GEOPHYSICS
2020, VOL. 9, NO. 1, 491–498
https://doi.org/10.1080/20909977.2020.1783633

Improving the performance of GNSS kinematic point positioning technique by simulated data

A. Lotfy, M. A. Abdelfatah and H. Hosny

Construction Engineering & Utilities Department, Faculty of Engineering, Zagazig University, Zagazig, Egypt

ABSTRACT

The aim of this research is intended to evaluate and improve the accuracy of point positioning technique. The basic point positioning model has been evaluated. Developed kinematic point positioning technique was proposed. A test was carried out to check the proposed method. The raw data was taken from real observed rover data and simulated base data. International Global Navigation Satellite System (GNSS) Service (IGS) final products were used in generating data of simulated base. The results show that using simulated base data can improve the accuracy of point positioning technique by 75 % and 72 % in horizontal and vertical components respectively.

ARTICLE HISTORY
Received 20 March 2020
Revised 4 June 2020
Accepted 10 June 2020

KEYWORDS
Simulation; GNSS; point positioning; kinematic

1. Introduction

The Point Positioning (PP) technique assumes that worldwide coherent satellite orbits and clocks are fixed or severely restricted and that PP mathematical models are compatible with those used in worldwide network alternatives from which the orbit/clock products have been estimated (Kouba et al. 2017). The PP is code measurements used to compute receiver position directly where the receiver's coordinates at an unknown point were sought with respect to the earth's reference frame by using the known positions of GNSS satellites being tracked. Also identified as absolute positioning (Kaartinen et al. 2015). At relative positioning, the receiver's coordinates at an unknown point were sought with respect to a receiver at a known point using code and carrier measurements (El-Rabbany 2002). The baseline was calculated from a known location to an unknown location. The term differential positioning was sometimes used with comparative positioning interchangeably. However, differential positioning was more frequently connected with a particular form of comparative positioning that applies corrections measured at a known location to unknown location measurements (He et al. 2014). GNSS positioning may also be categorised as static or kinematic. In static positioning, a GNSS receiver was required to be stationary whereas in Kinematic positioning a receiver collect GNSS data while moving as shown in Figure 1(a,b). For Kinematic relative positioning, one receiver, known as a base, was left stationary at a known point while a second receiver, known as a rover, is shifted over the route to be positioned (Colombo et al. 2004).

Depending on the implementation and user dynamics, autonomous PP positions are estimated in kinematic mode at each observation epoch, typically every 1 – 30 s (Chen et al. 2004). If observation intervals are shorter than the sampling of the satellite clock, clock interpolation is required. Due to the instability of the satellite clock, only clocks at a sampling interval of 30 s or lower can be interpolated reliably at the precision level of cm. IGS and most IGS AC clock alternatives presently use 30 sampling, but higher-rate clock products can be provided for specific apps by individual analytical centres (Bock et al. 2009).

In most commercial and scientific applications of GNSS kinematic positioning, differential positioning is used with data from a reference station and a rover receiver (Furones et al. 2012). The primary issue with double differencing positioning, however, is that the amount of residual errors rises as the distance between the reference and the rover receiver increases. An alternative strategy is point positioning (PP). Point positioning can provide accuracy of positioning submeter to centimetre using only one carrier-phase GNSS receiver, that is, without the use of base stations, it reduces the cost of the GNSS survey (Lotfy 2019). PP uses high-resolution carrier phase and pseudorange observations in processing algorithms where precise satellite orbits and clock data are used instead of broadcasting data (Li et al. 2012).

Through the availability of the IGS real-time service, accurate orbit and satellite clock corrections can be obtained in real time through greater precision than that of the ultra-rapid (predicted part) products. The RTS products are shown to be superior to the ultra-rapid ones. In addition, using IGS RTS products in

CONTACT A. Lotfy ahmed.lotfy1164@yahoo.com Construction Engineering & Utilities Department, Faculty of Engineering, Zagazig University, Zagazig, Egypt

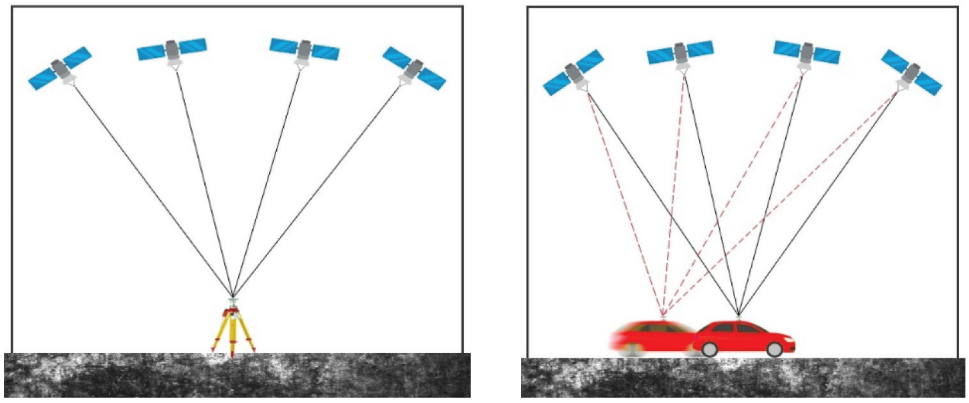

a b

Figure 1. (a). Static single point positioning. (b). Kinematic single point positioning.

real time PPP can improve the solution RMS by about 50 % compared with the solution that obtained from the predicted part of the IGS ultra rapid products (Elsobeiey and Al-Harbi 2015).

The accuracy of the point positioning was assessed using data from different test data sets, including fixed receivers at known points and a moving receiver installed on a van. So, the objectives of this research are improving the performance of kinematic point positioning technique by using simulated base data and compared with real base data.

2. Testing area and data collection

The testing areas of this research were in 10th of Ramadan city and Enshas. Five routes were observed in 10th of Ramadan city and three routes were in Enshas as shown in Figure 2(a–h). Two GNSS receivers were used with brand ComNav T300 PLUS (observed GPS, GLONSS, GALILIO and BEIDU). One receiver was rover and another one was a base station as summarised in Table 1 to obtain real data for comparing the performance with simulated data. The rover was fixed on a vehicle and was derived from observed data as summarised in Table 2.

Three different cases of this data were studied by observations of GNSS. The first case was the study of data that were observed by the rover only and was solved as a point positioning (PP). As for the second case, the base observations were generated by using a simulated (SIMU) base station in the same position as the real one created by Bernese GNSS software using GPS ephemeris only, and then they were solved with the observations of the rover. As for the third case, the observations obtained from the rover and the real base station were used, and they were resolved in a differencing technique (Diff) using the BERNESE softwareV.5. After that, these cases were compared.

3. Mathematical model of kinematic network

3.1. Point positioning

3.1.1. Code range model

The code pseudorange at an epoch t can be modelled by:

$$R_r^s(t) = \varrho_r^s(t) + c\Delta\delta_r^s(t) \tag{1}$$

Where

$R_r^s(t)$ is the pseudorange code measured between the receiver site r and the satellite s.

$\varrho_r^s(t)$ is the geometric distance between the observing point and the satellite.

c is the speed of light.

$\Delta\delta_r^s(t)$ is clock bias representing the combined clock offsets of the receiver and the satellite clock with respect to system time.

Examining Equation (1), the desired coordinates of the receiver site to be determined are implicit in the distances $\varrho_r^s(t)$ (Hofmann-Wellenhof et al. 2007), which can explicitly be written as:

$$\varrho_{r(t)}^s(t) = \sqrt{\begin{matrix}\left(X^s(t) - X_{r(t)}\right)^2 + \left(Y^s(t) - Y_{r(t)}\right)^2 \\ +\left(Z^s(t) - Z_{r(t)}\right)^2\end{matrix}} \tag{2}$$

Where

$X^s(t), Y^s(t), Z^s(t)$ are components of the satellite's geocentric position vector at epoch t.

$X_{r(t)}, Y_{r(t)}, Z_{r(t)}$ are the three cartesian coordinates of the (stationary) observing receiver site.

3.1.2. Phase range model

Pseudoranges can also be obtained from carrier phase measurements (Hofmann-Wellenhof et al. 2007). The mathematical model for these measurements is given by

$$\phi_r^s(t) = \frac{1}{\lambda^s}\varrho_r^s(t) + N_r^s + \frac{C}{\lambda^s}\Delta\delta_r^s(t) \tag{3}$$

Where

Figure 2. (a). Map of route 1 (R1). (b). Map of route 2 (R2). (c). Map of route 3 (R3). (d). Map of route 4 (R4). (e). Map of route 5 (R5). (f). Map of route 6 (R6). (g). Map of route 7 (R7). (h). Map of route 8 (R8).

Table 1. The accurate values of stations` coordinates.

Station	Code	Northing (φ)	Easting (λ)	Height (h)	Receiver Type
Enshas	ENS	30°20′39.290″	31°26′31.659″	33.65	ComNav T300P
10th of Ramadan	ASH	30°17′46.027″	31°44′14.972″	133.83	ComNav T300P

$\phi_r^s(t)$ is the measured carrier phase expressed in cycles.

λ^s is the wavelength.

$\varrho_r^s(t)$ is the same as for the code range model.

N_r^s is an integer ambiguity.

C denotes the speed of light.

$\Delta_r^s(t)$ is the combined receiver and satellite clock bias.

Inserting Equation (1) into Equation (3) and shifting the (known) satellite clock bias to the left side of the equation yields

Table 2. Number of epochs in each route.

Route no.	Length (km)	No. of epochs	Base stations
R1	15	4190	10th of Ramadan City
R2	10	1915	
R3	10	4719	
R4	12	4144	
R5	12	4609	
R6	4	9376	Enshas
R7	7	17643	
R8	6	12150	

$$\phi_r^s(t) + f^s\delta^s(t) = \frac{1}{\lambda^s}\varrho_r^s(t) + N_r^s + f^s\delta_r(t) \quad (4)$$

where the frequency of the satellite carrier $f^s = {}^c/_{\lambda^s}$ has been substituted.

3.2. Simulation PP model

This model was created to obtain simulation base data. The coordinates of simulated receiver and satellite were known and the distance between them was unknown. The positioning equation can be expressed by:

$$P = f(O,\ E\ and\ \Delta)$$

Where P is positioning, O is observation, E is ephemeris and Δ is errors. During the simulation, the inverse of this equation is used:

$$O = f(P, E\ and\ \Delta)$$

The mathematical model for these measurements is given by:

$$Q_{r(t)}^s(t) = \sqrt{\begin{matrix}(X^s(t) - X_r)^2 + (Y^s(t) - Y_r)^2 \\ +(Z^s(t) - Z_r)^2\end{matrix}} \quad (5)$$

where

$X^s(t), Y^s(t), Z^s(t)$ are components of the satellite's geocentric position vector at epoch t.

X_r, Y_r, Z_r are the three cartesian coordinates of the simulated receiver site.

The coordinates of satellites were known from IGS final products.

$$\lambda^s\phi_r^s(t) = \varrho_r^s(t) + \lambda^s N_r^s + \Delta\delta_r(t) \quad (6)$$

$$l = Ax + V \quad (7)$$

The linearisation is performed for $\varrho_r^s(t)$ and known terms are shifted to the left side. Multiplying Equation 6 by λ and using $c = \lambda f$ yields:

$$\begin{aligned}\lambda\phi_r^s(t) - \varrho_{r0}^s(t) + c\delta^s(t) = &-\frac{X^s(t) - X_{r0}}{\varrho_{r0}^s(t)}\Delta X_r \\ &-\frac{Y^s(t) - Y_{r0}}{\varrho_{r0}^s(t)}\Delta Y_r \\ &-\frac{Z^s(t) - Z_{r0}}{\varrho_{r0}^s(t)}\Delta Z_r + \lambda N_r^s \\ &+ c\delta_r(t)\end{aligned} \quad (8)$$

Considering again four satellites, the system is given in matrix-vector form L = A*x (Hofmann-Wellenhof et al. 2007), where

$$l = \begin{bmatrix}\lambda\phi_r^1(t) - \varrho_{r0}^1(t) + c\delta^1(t) \\ \lambda\phi_r^2(t) - \varrho_{r0}^2(t) + c\delta^2(t) \\ \lambda\phi_r^3(t) - \varrho_{r0}^3(t) + c\delta^3(t) \\ \lambda\phi_r^4(t) - \varrho_{r0}^4(t) + c\delta^4(t)\end{bmatrix} \quad (9)$$

$$A = \begin{bmatrix}a_{X_r}^1(t) & a_{Y_r}^1(t) & a_{Z_r}^1(t) & \lambda & 0 & 0 & 0 & c \\ a_{X_r}^2(t) & a_{Y_r}^2(t) & a_{Z_r}^2(t) & 0 & \lambda & 0 & 0 & c \\ a_{X_r}^3(t) & a_{Y_r}^3(t) & a_{Z_r}^3(t) & 0 & 0 & \lambda & 0 & c \\ a_{X_r}^4(t) & a_{Y_r}^4(t) & a_{Z_r}^4(t) & 0 & 0 & 0 & \lambda & c\end{bmatrix} \quad (10)$$

$$x = \begin{bmatrix}\Delta X_r & \Delta Y_r & \Delta Z_r & N_r^1 & N_r^2 & N_r^3 & N_r^4 & \delta_r(t)\end{bmatrix}^T \quad (11)$$

Thus, simulated data can be obtained.

The code observations by

$$\frac{C}{A}code = \varrho_1 + \Delta_1 \quad (12)$$

$$pcode = \varrho_2 + \Delta_2 \quad (13)$$

The phase observations by

$$L_1 = \lambda_1\phi_1 + \Delta_3 \quad (14)$$

$$L_2 = \lambda_2\phi_2 + \Delta_4 \quad (15)$$

The solution of this redundant system is performed by least-squares adjustment to create simulated RINEX data as seen in Figure 3. These processes were completed using the GNSS softwareV.5.

4. Results and discussion

Data was solved by using the BERNESE software V.5 to analyse the kinematic point positioning for all routes. The data of simulated base was generated for all routes to improve the performance of point positioning technique. Horizontal axis refers to an error in millimetres and the vertical axis refers to the routes.

4.1. Horizontal components

There are 8 routes for testing the model which are divided into five routes in 10th of Ramadan city and three routes in Enshas.

The chart in Figure 4 shows that the easting's error values in millimetres. In route 2, by using PP the error value was 1267 mm and when using data of simulated base, the error value became 456 mm. In route 3, by using PP the error value was 1609 mm and when using data of simulated base, the error value became 360 mm. In route 4, by using PP the error value was 476 mm and when using data of simulated base, the error value

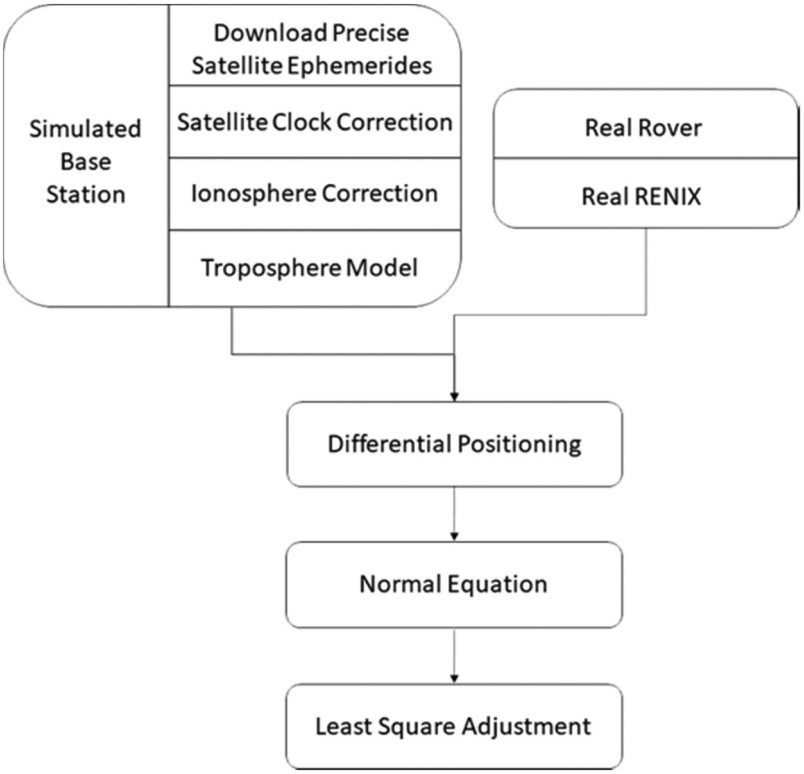

Figure 3. The processes of simulation for kinematic point positioning.

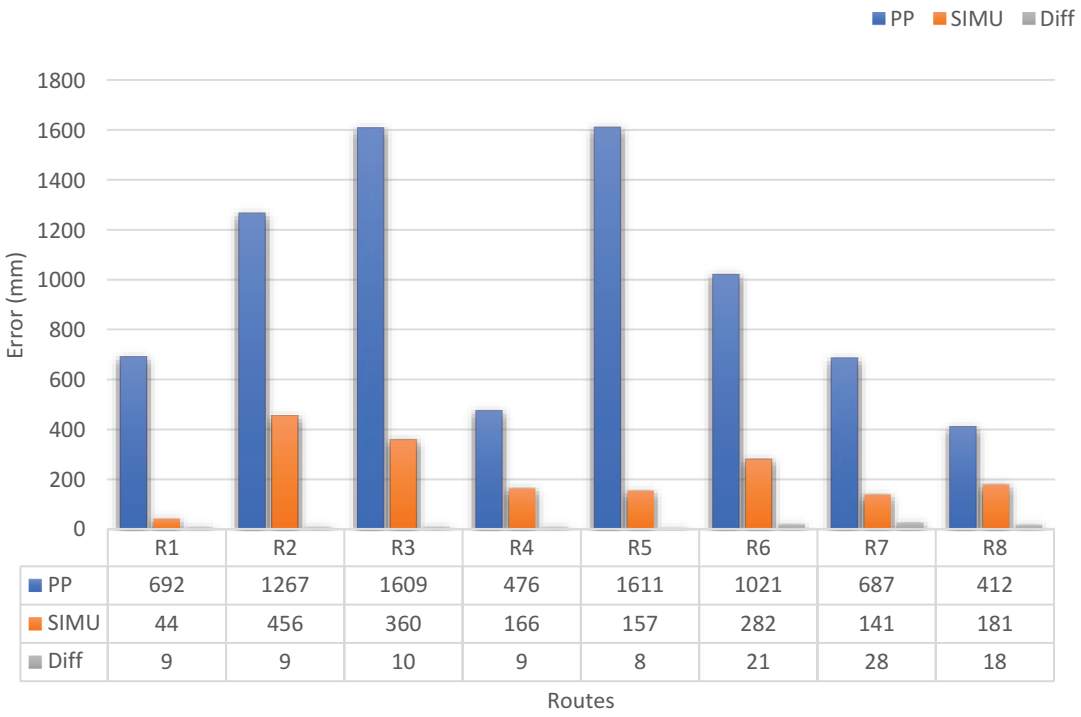

	R1	R2	R3	R4	R5	R6	R7	R8
PP	692	1267	1609	476	1611	1021	687	412
SIMU	44	456	360	166	157	282	141	181
Diff	9	9	10	9	8	21	28	18

Figure 4. The error of easting for all routes in (mm).

became 166 mm. In route 5, by using PP the error value was 1611 mm and when using data of simulated base, the error value became 157 mm. In route 6, by using PP the error value was 1021 mm and when using data of simulated base, the error value became 282 mm. In route 7, by using PP the error value was 687 mm and when using data of simulated base, the error value became 141 mm. In route 8, by using PP the error value was 412 mm and when using data of simulated base, the error value became 181 mm.

Figure 5 shows that the northing's error values in millimetres. In route 2, by using PP the error value was

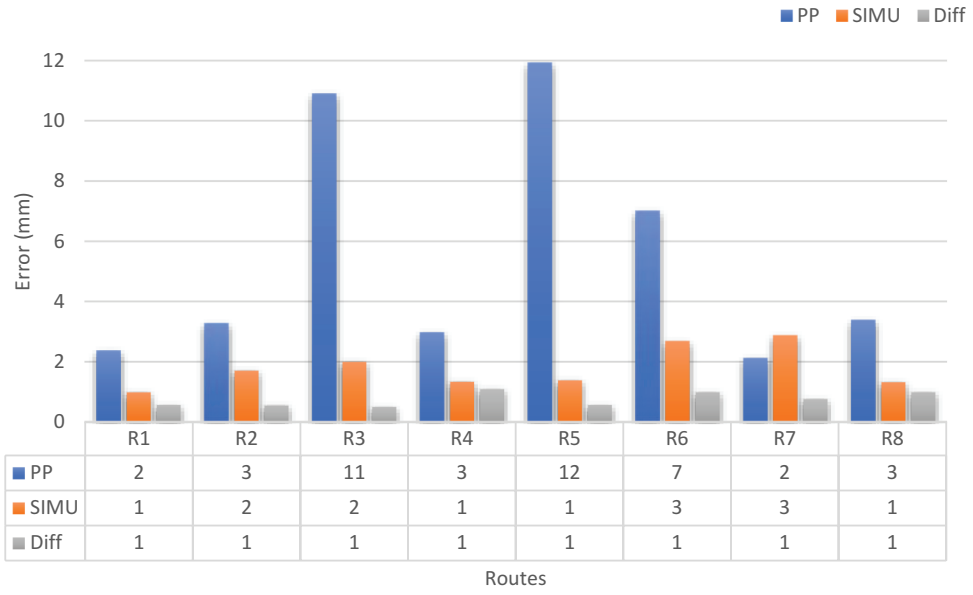

Figure 5. The error of northing for all routes in (mm).

3 mm and when data of simulated base the error value became 2 mm. In route 3, by using PP the error value was 11 mm and when using data of simulated base, the error value became 2 mm. In route 4, by using PP the error value was 3 mm and when using data of simulated base, the error value became 1 mm. In route 5, by using PP the error value was 12 mm and when using data of simulated base, the error value became 1 mm. In route 6, by using PP the error value was 7 mm and when using data of simulated base, the error value became 3 mm. In route 7, by using PP the error value was 2 mm and when using data of simulated base, the error value became 3 mm. In route 8, by using PP the error value was 3 mm and when using data of simulated base, the error value became 1 mm. From the previous charts show that the percentage of improving by using data of simulated base for horizontal components was 75 %. The errors in IGS simulation data are reduced due to the use of the differencing technique despite the use of one real rover.

As shown, the length of the route and the number of epochs have a great impact on increasing accuracy. When increasing the length of the route with movement at a low speed leads to an increase in the number of epochs and consequently increases accuracy. In addition to the effect of the observing location, 10th of Ramadan city is an urban area, which a clear sky view with no obstructions nor nearby huge constructions, so the accuracy of the observations is high, even though the number of epochs has less than Enshas because it is a non-urban area, that has high constructions, obstructions, and narrower views according to the view of the antenna, so the number of epochs in it must be increased to obtain acceptable accuracy. Knowing that the GDOP upper limit was not increasing than two in all cases.

4.2. Vertical components

The chart in Figure 6 shows that the height's error values in millimetres. In route 2, by using PP the error value was 924 mm and when using data of simulated base, the error value became 244 mm. In route 3, by using PP the error value was 922 mm and when using data of simulated base, the error value became 272 mm. In route 4, by using PP the error value was 648 mm and when using data of simulated base, the error value became 253 mm. In route 5, by using PP the error value was 830 mm and when using data of simulated base, the error value became 212 mm. In route 6, by using PP the error value was 902 mm and when using data of simulated base, the error value became 294 mm. In route 7, by using PP the error value was 915 mm and when using data of simulated base, the error value became 278 mm. In route 8, by using PP the error value was 912 mm and when using data of simulated base, the error value became 276 mm. From the previous charts show that the percentage of improving by using data of simulated base for vertical components was 72 %.

4.3. Test of hypothesis for two sample means (T-Test)

The two-sample t-test has been performed on the results of processed data of all routes. In this test, the two-sample means are compared. The two hypotheses; null hypothesis, H0, and alternative hypothesis, Ha, are stipulated as follows:

$$H_0 : \mu_1 \neq \mu_2 \tag{16}$$

$$H_a : \mu_1 = \mu_2 \tag{17}$$

The test statistic is

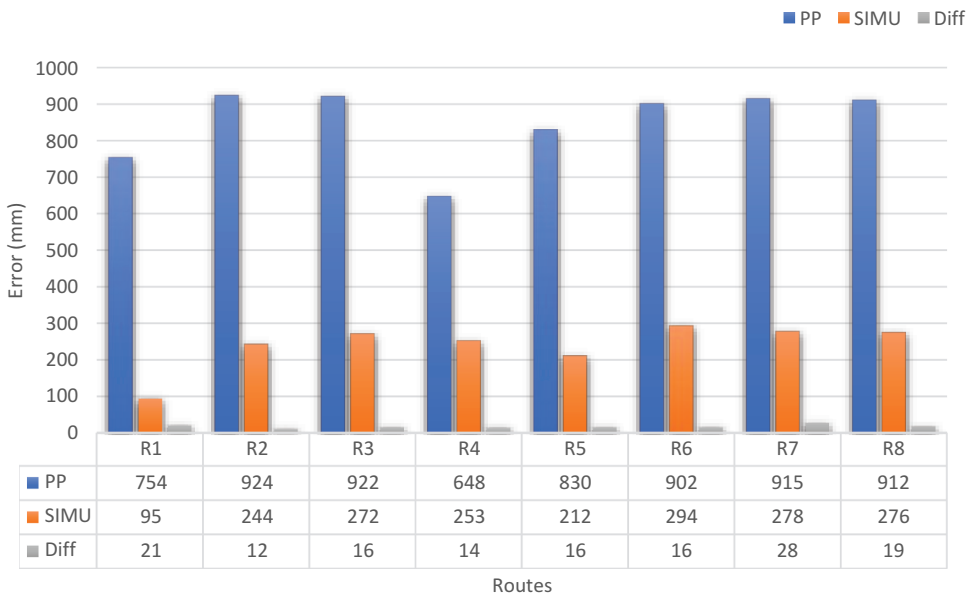

Figure 6. The error of height for all routes in (mm).

Table 3. T-test for different cases.

	PP		SIMU	
Parameter	T-test	Status	T-test	Status
Easting	1.99	rejected	1.56	accepted
Northing	1.07	accepted	0.85	accepted
Height	2.78	rejected	1.17	accepted

$$T = \frac{\bar{Y}_1 - \bar{Y}_2}{\sqrt{\frac{S_1^2}{N_1} + \frac{S_2^2}{N_2}}} \tag{18}$$

The null hypothesis is rejected in the region:

$$|T| < T_{\alpha/2}$$

Where $\bar{Y}_1$ and $\bar{Y}_2$ are the means of the samples, S_1^2 and S_2^2 are the variances, N_1 and N_2 are the sample sizes and $t_{\alpha/2}$ are the tabulated t-value at confidence level 95%.

Table 3 is showing the values of the t-test for the three parameters; easting, nothing, and height. The T-test here is implemented for two cases; point positioning (PP) and simulation (SIMU) with difference method (Diff). The tabulated value of t is 1.96 at a confidence level of 95%. The values of the t-test smaller than the tabulated value are accepted and greater than the tabulated value is rejected.

5. Conclusions

With the availability of the IGS services, it will be easy to obtain high accuracy in kinematic point positioning applications. Based on the previous results of kinematic point positioning and data of the simulated base, the following can be concluded:

In the horizontal component, the accuracy of kinematic point positioning was 972 mm and when using the proposed technique of simulated base was 223 mm with improving percentage 77%. In vertical component, the accuracy of kinematic point positioning was 851 mm and when using the proposed technique of simulated base was 250 mm with improving percentage 72%. Considering, the effect of both the route length, the number of epochs, and the observation location, because by increasing the number of epochs and observed in urban areas, accuracy increases. After using the statistical tests, the point positioning case was rejected in easting and height.

Disclosure statement

No potential conflict of interest was reported by the authors.

ORCID

A. Lotfy http://orcid.org/0000-0003-2004-4206

References

Bock H, Dach R, Jäggi A, Beutler G. 2009. High rate GPS clock corrections from CODE: support of 1 Hz applications. J Geod. 83(11):1083. doi:10.1007/s00190-009-0326-1.

Chen W, Hu C, Li Z, Chen Y, Ding X, Gao S, Ji S. 2004. Kinematic GPS precise point positioning for sea level monitoring with GPS Buoy. J Global Positioning Sys. 3 (1–2):302–307. doi:10.5081/jgps.3.1.302.

Colombo OL, Sutter AW, Evans AG. 2004. Evaluation of Precise Kinematic GPS Point Positioning. In: Proceedings of ION GNSS 17th International Technical Meeting of the Satellite Division, Long Beach; California. P. 1423–1430.

El-Rabbany A. 2002. Introduction to GPS: the global positioning system. Artech House, USA. ISBN 1-58053-183-0.

Elsobeiey M, Al-Harbi S. 2015. Performance of real-time precise point positioning using IGS real-time service. GPS Solutions. 20(3):565–571. doi:10.1007/s10291-015-0467-z.

Furones M, Esteban A, Anquela AB, Berné V, Sanmartín M. 2012. Kinematic GNSS-PPP Results from Various Software Packages and Raw Data Configurations. Sci Res Essays. 7(3):419–431.

He H, Li J, Yang Y, Xu J, Guo H, Wang A. 2014. Performance assessment of single and dual frequency BeiDou/GPS single epoch kinematic positioning. GPS Solutions. 18 (3):393–403. doi:10.1007/s10291-013-0339-3.

Hofmann-Wellenhof B, Lichtenegger H, Wasle E. 2007. GNSS Global Navigation Satellite Systems: GPS, GLONASS, Galileo, and More. New York, NY: Springer Science and Business Media. ISBN 978-3-211-73012-6.

Kaartinen H, Hyyppä J, Vastaranta M, Kukko A, Jaakkola A, Yu X, Kaijaluoto R. 2015. Accuracy of kinematic positioning using global satellite navigation systems under forest canopies. Forests. 6(9):3218–3236. doi:10.3390/f6093218.

Kouba J, Lahaye F, Tétreault P. 2017. Precise point positioning. In: Teunissen PJ, Montenbruck O, editors. Springer Handbook of Global Navigation Satellite Systems. Cham: Springer. ISBN: 978-3-319-42926-7

Li B, Shen Y, Zhang X. 2012. Three frequency GNSS navigation prospect demonstrated with semi-simulated data. Adv Space Res. 51(7):1175–1185. doi:10.1016/j.asr.2012.10.031.

Lotfy A. 2019. Optimization Analysis for Improving the Performance of Regional Kinematic GNSS Networks [master thesis]. Egypt: Faculty of Engineering, Zagazig University.